ANNALS OF GEOPHYSICS, 68, 2, V225, 2025; doi:10.4401/ag-9188
OPEN ACCESS

A study on the effects of effusion rate on 2D numerical simulations of lava flow evolution

Eleonora Amato[*,1,2]

(1) Istituto Nazionale di Geofisica e Vulcanologia, Sezione di Catania, Osservatorio Etneo, Catania, Italy
(2) University of Palermo, Department of Mathematics and Computer Science, Palermo, Italy

Article history: received October 19, 2024; accepted March 27, 2025

Abstract

The effusion rate plays a crucial role in controlling the evolution of volcanic eruptions and it is thus critical to quantify the associated volcanic hazards. It represents the volume of lava emitted over time and can be estimated using satellite remote sensing data, such as Volcanic Radiative Power (VRP) measurements, deriving the Time Averaged Discharge Rate (TADR). Variations in the effusion rate can influence the resulting eruption style, ranging from effusive or Strombolian to lava fountaining activity. Thanks to the abundance of free data collected through fieldwork and remote sensing, it is now possible to numerically simulate eruptive behaviors with Computational Fluid Dynamics (CFD) models, allowing for a detailed study of lava flow evolution in time and space, without the dangers of collecting field data. We have already largely simulated lava flows with a Lagrangian mesh-free particle CFD method, known as Smoothed Particle Hydrodynamics (SPH). This model takes in input the physical parameters of the fluid and returns in output a numerical simulation of its spatio-temporal evolution. Here, we propose a framework to simulate lava flows with a range of values for some physical parameter, to better understand their results on numerical simulations, bringing to a deeper knowledge of the different eruptive behaviors in function of these parameters. In particular, we conduct a study on the effusion rate effects over 2D numerical simulations of lava using numerical physical-mathematical models that return as output not only the evolution of the flow front but also the behavior of the vertical flow section. Using the TADR derived from VRP data and the SPH method, we simulate the fluid flow under different effusion rate conditions. This sensitivity analysis demonstrates how varying effusion rates affect the evolution of the flow front and vertical cross-section. In detail, we show how time-independent and time-dependent effusion rates, obtained by satellite data, can make possible to qualitatively analyze and reproduce different eruptive styles, as effusive, Strombolian, or explosive activity and variable flows. The results highlight the potential for integrating real observations with numerical models and lay the groundwork for future applications that combine these approaches with artificial intelligence to enhance the model performance.

Keywords: Effusion rate, Time Averaged Discharge Rate (TADR), Lava, Computational Fluid Dynamics (CFD), Smoothed Particle Hydrodynamics (SPH)

1. Introduction

Volcano monitoring involves both tracking ongoing eruptions and forecasting areas that can be affected by volcanic hazards (Cappello et al., 2018; Del Negro et al., 2020; Harris, 2013). Accurately quantifying the hazard associated with an active volcano is a complex task, particularly because it requires advanced models to describe volcanic phenomena and relies heavily on both direct and remote sensing observations (Cappello et al., 2013). Recent approaches have combined field observations with remote sensing data, along with analytical, statistical, and probabilistic models, as well as artificial intelligence techniques, to study the trends of hazardous volcanic events in space and time, applying these models to a variety of dangerous volcanic phenomena, including pyroclastic flows (Alberico et al., 2002; Calvari et al., 2020), ash clouds and volcanic plumes (Corradini et al., 2023; Torrisi et al., 2022, 2024), thermal anomalies, lava flows and tephra fallout (Amadio et al., 2024; Amato et al., 2023a; Del Negro et al., 2022; Scollo et al., 2024; Corradino et al., 2024; Malaguti et al., 2024), which often interact with the surrounding environment (Cioni et al., 2023).

One of the main parameters used to describe the volcanic effusive eruptions and quantify the associated hazards is the effusion rate, which is the volume of lava emitted per unit of time (m^3/s). Rather than relying solely on field measurements, the effusion rate can be estimated through remote sensing techniques, such as satellite data. Specifically, satellites can capture the Earth's spectral response, which changes over time in terms of different physical and chemical characteristics (Amato et al., 2023b). Different satellite sensors provide an estimation of the Volcanic Radiative Power (VRP) (W), a parameter widely used to estimate the effusion rate during volcanic eruptions (Coppola et al., 2012; Di Bella et al., 2024; Torrisi et al., 2023). VRP represents the radiative heat power emitted by an incandescent surface, in particular volcanic lava flows, and it is calculated based on the lava flow area and the relative temperature (Harris, 2013; Harris et al., 2007; Wooster et al., 2005). Satellite data can be processed using different methodologies, such as the Middle InfraRed (MIR) method (Wooster, 2003). This method can be used to extract VRP values (Vicari et al., 2011; Corradino et al., 2019) from the Spinning Enhanced Visible and InfraRed Imager (SEVIRI) sensor, which is on board the Meteosat Second Generation (MSG) satellite operated by ESA EUMETSAT (Amato, 2022; Amato et al., 2021). The Time Averaged Discharge Rate (TADR) (m^3/s) is derived from VRP and represents the averaged lava extrusion rate over a given time period (Coppola et al., 2013). TADR can be multiplied by the duration of the eruption to estimate the total volume of erupted lava (Harris, 2013), or used alongside other volcanic parameters, such as lava flow area of the erupted lava, to estimate the thickness of lava deposits (Harris, 2013). TADR can also serve as an input parameter for numerical or statistical models used to study and simulate the evolution of (effusive) eruptive events, also with lava fountaining or similar activity (Amato et al., 2021; Corradino et al., 2021, 2022; Hérault et al., 2011; Zuccarello et al., 2022).

Several studies have examined volcanic activity based on the eruption rate (the volumetric discharge rate averaged over the eruption) and the effusion rate. For example, (Wadge, 1978, 1981) showed that the discharge rate during a basaltic eruption follows an asymmetric trend, where the growth phase is shorter than the waning phase, with a linear trend of decreasing eruption rate with increasing duration of the eruption, but also a linear relationship between effusion rate and lava flow maximum distances has been recognized. (Wadge, 1978, 1981) also showed the possibility to extrapolate a fitting curve with an exponential decreasing behavior to model the waning phase of an eruption. Moreover, (Calvari and Pinkerton, 1998) found that the eruption rate directly affects specific eruption characteristics, such as the final flow length, size, and lava tube formation.

Given the primary role of effusion rate in eruption dynamics, there has been significant motivation to characterize its common trends. Some authors (Coppola et al., 2009, 2017; Harris et al., 2011, 2000) classified four different types of effusion rate curves from TADR, while others authors (Aravena et al., 2018, 2020) have analyzed the physical properties of volcanic systems to investigate the effect of different parameters (specifically, the size of the magma reservoir, its initial overpressure, the dimensions of the feeding dike, and its feeding coefficient) on effusion rate trends. Analyses like these provide statistical insights that help to better understand the outcomes of numerical models, revealing different eruptive behaviors when input parameters are varied.

Other studies have applied Cellular Automata models to evaluate the impact of physical and rheological parameters. These models have been used to verify reliability and forecast possible future scenarios, producing robust results regarding the effect of effusion rate on lava emplacement (Bilotta et al., 2012). Subsequent works have implemented a similar approach by combining field data, numerical simulations, and probability analyses to obtain lava flow hazard maps of areas susceptible to be affected by these volcanic phenomena (Del Negro et al., 2020; Zuccarello et al., 2023). By considering the distribution of eruption durations and lava volumes, and their relationship,

it has been also possible to classify six eruptive styles to be used as input parameters in numerical simulations of lava flows (Vicari et al., 2011, 2007).

Here, we present a study on the effects of effusion rate on 2D numerical simulations of lava flows in the (x, z) Cartesian plane. These simulations are capable of modeling not only the evolution of the flow front but also the behavior of the vertical flow section. We used an analytical formulation for the TADR, directly estimated from satellite remote sensing VRP data, to exploit the advantages of using freely-accessible data without dangers linked to direct observations and measurements. We also employed a Lagrangian mesh-free particle method to faithfully simulate the fluid flow. In particular, we focused on the recent eruptive activity of Mount Etna (Sicily, Italy), which consisted of six eruptions at the Voragine summit crater between July and August 2024 (Calvari and Nunnari, 2024), with eruptive style ranging from Strombolian to lava fountaining. SEVIRI VRP satellite data were collected and analyzed for each eruption, allowing us to calculate the TADR and derive the corresponding fitting curves. By observing similar patterns in the effusion rate trends, we combined all these fitted curves to produce a single averaged trend representative of the behavior of this eruptive phase of Mt. Etna. This averaged curve was then used as input of a numerical Computational Fluid Dynamics (CFD) model, based on the Smoothed Particle Hydrodynamics (SPH) method, to simulate the evolution of a fluid with lava-like characteristics. Starting with lava simulations with fixed values of effusion rate, thereby, we aim to model a visco-thermal fluid with a time-variable effusion rate, mimicking the conditions observed in real case studies. It is worth to note that the numerical model does not seek to exactly replicate the physical phenomenon but instead aims to qualitatively explore the effects of effusion rate on the simulation. This can provide an example of a time-varying effusion rate and its influence on fluid emplacement. This study lays the groundwork for future developments integrating numerical models with field and remote sensing data (thermal and visible cameras or satellite observations), creating a model capable of reproducing real case studies. Such a framework could be applied to monitor volcanic systems, track ongoing eruptions, and estimate possible future scenarios, ultimately aiding in the quantification of volcanic hazards.

2. Eruptions analyzed

Data used in this work were sampled from the eruptive activity of Mount Etna (Sicily, Italy) (Fig. 1) in the summer 2024. After a long period of rest, during June 2024 the summit crater Voragine resumes its activity with mild Strombolian activity. This activity then evolves producing six paroxysmal events in the period between July and August 2024 (previous Voragine crater explosive sequences occurred in December 2015 and May 2016). Chemical analysis carried out on the erupted materials highlights a first phase with a more evolved magma (June activity), followed by a more primitive magma feeding the first and second lava fountains (Calvari and Nunnari, 2024). All these eruptions follow a similar trend, with lava fountaining generating high eruptive columns preceded and followed by Strombolian activity and lava flow emplacement. Table 1 shows the total duration of the events ("eruption date", which includes different eruptive styles, as strombolian activity, lava fountains, or overflow), the onset of the lava fountain events only (which are the ones studied in this work), with starting and ending time, the volume and maximum TADR values from satellite data and the eruptive style of the entire eruptions (in chronological order). All these events present a lava overflow, which generates a lava field, for which it is therefore legitimate to calculate the TADR (in addition to the VRP). All these data are derived from INGV (Istituto Nazionale di Geofisica e Vulcanologia) weekly bulletins, at www.ct.ingv.it.

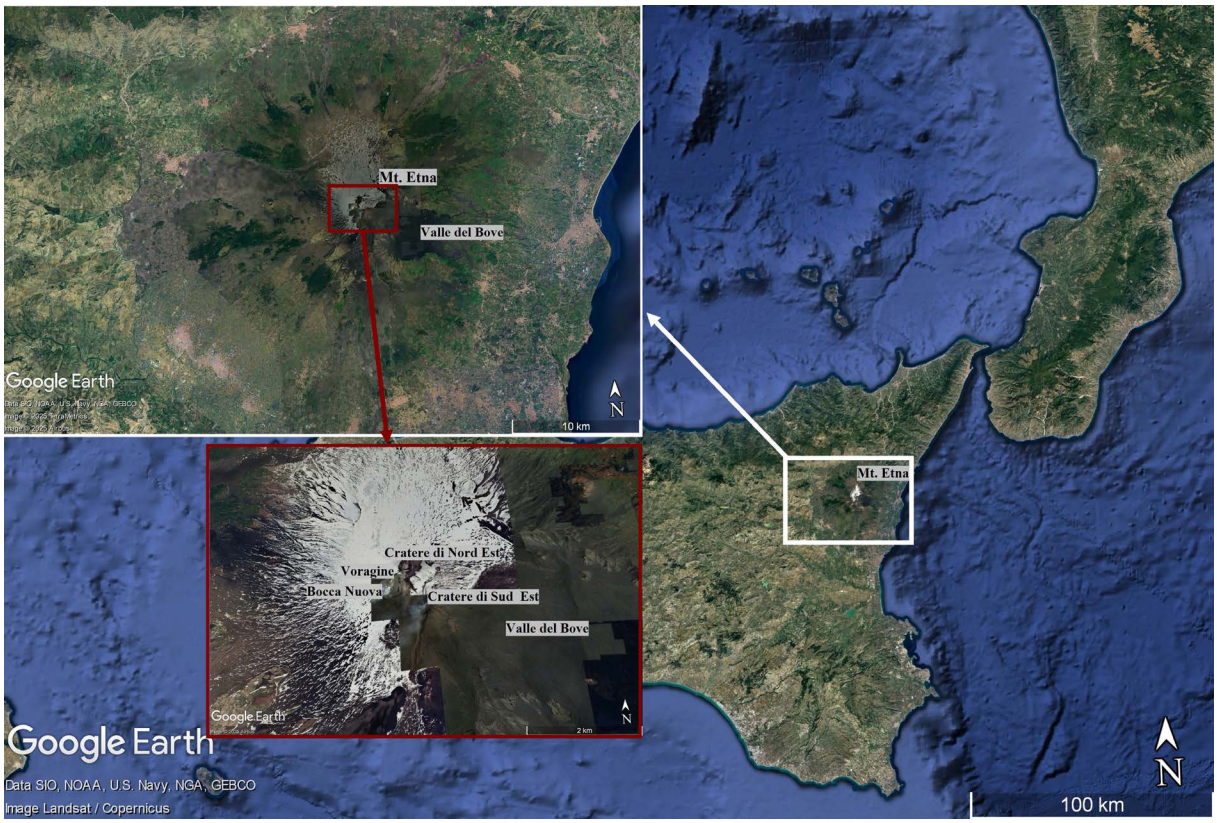

Figure 1. Location of the Mt. Etna volcano (white boxes), in Sicily, Italy, and the summit craters (red boxes, North-East Crater/Cratere di Nord-Est, Voragine, Bocca Nuova, South-East Crater/Cratere di Sud-Est), with the valley in the east part of the volcano itself (Valle del Bove), where the lava frequently flows.

Eruption date	Lava fountain start (UTC)	Lava fountain end (UTC)	Volume	Max TADR (from satellite)	Eruptive style
04-05 July 2024	16:50	01:21	0.64×10^6 m^3	21 m^3/s ± 9 m^3/s	S – LF – O – S
07 July 2024	01:54	07:23	0.43×10^6 m^3	27 m^3/s ± 12 m^3/s	S – LF – O – S – AD
15 July 2024	18:24	00:17	0.41×10^6 m^3	18 m^3/s ± 9 m^3/s	S – LF – O – S
22-23 July 2024	05:43 (23 July)	08:00	0.5×10^6 m^3	16 m^3/s ± 7 m^3/s	S – AD – LF – O
04 August 2024	02:19	08:12	0.45×10^6 m^3	27 m^3/s ± 13 m^3/s	S – LF – O
14-15 August 2024	21:33	01:29	0.40×10^6 m^3	18 m^3/s ± 9 m^3/s	S – LF – O – E – S

Table 1. Eruptions parameters, data obtained from INGV weekly bulletins at www.ct.ingv.it and (Calvari and Nunnari, 2024) (in "Eruptive style" column, S: Strombolian, LF: Lava Fountain, O: Overflow, AD: Ash Dispersion (fallout), E: Explosion).

3. Method

We apply a two-step approach, in which firstly the satellite data are used to estimate the parameters linked to the eruptive style and, subsequently, these parameters are used in the numerical model to simulate the volcanic activity. Results do not exactly replicate the real physical phenomena analyzed, but they aim to reproduce the qualitative behavior of the eruptions varying the effusion rate values, starting from the July-August 2024 Mt. Etna activity. We used time-constant and time-dependent effusion rates, obtained by satellite data, to evaluate their effect on the simulation trend and on the relative emplacement of the lava flow. We choose to use effusion rates from satellite to take advantage from the great quantity of free and accessible data, without dangers linked to in field measurements.

3.1 First step: effusion rate fitting curve estimation

For each eruption listed in Table 1, we used the VRP satellite data from the SEVIRI MSG satellite and analyzed the signals for the entire duration of the eruption. We converted each VRP data point (W) to TADR (m^3/s) using the formulas in Eqs. (1-2), which take into account the lava content of silica, estimated as $X_{SiO2} = 47.9$ wt% for Mt. Etna (Coppola et al., 2013; Harris, 2013; Plank et al., 2019, 2021),

$$TADR = \frac{VRP}{C_{rad}} \tag{1}$$

$$C_{rad} = \frac{6.45 \cdot 10^{25}}{X_{SiO_2}^{10.4}} \tag{2}$$

Equations (1-2) show the empirical relationship between the VRP, in $W = J\ s^{-1}$, and the C_{rad} constant ($J\ m^{-3}$), named the radiant density, which is function of the percentage of silica content in the lava analyzed. The radiant density, for a given discharge rate, is the amount of thermal energy radiated per unit volume of active lava (Coppola et al., 2013), and it follows the lava body changes in area and variation in the inner core.

Finally, we consider the TADR values in time for each eruption listed in Table 1 and calculate a fitting curve to obtain a time-dependent function to describe the TADR behavior. In particular, for each eruption we have applied some preprocessing techniques to prepare the data for the fitting, identifying the missing values and substituting them with null values (being mostly the values in the initial and final queues), necessary step for the correct use of the fitting method. Subsequently, we applied a non-linear least squares to fit a function $f(t)$ for the TADR data (defined as f function of time t) (Vugrin et al., 2007). We define a Lorentzian functional form (Jain et al., 2018) as in Eq. (3), with parameters amplitude (A), width (w), and center (c) to be defined, choosing to use the Lorentzian curve (LC), and not the more common Gaussian one (GC), because the LC is narrower around the center and extends more respect to the GC on the sides, following in a better way the data under analysis

$$f(t) = \frac{A^2 w^2}{(t-c)^2 + w^2} \tag{3}$$

We have repeated the same procedure for each eruption, obtaining a final averaged fitting curve for the TADR.

We add in the simulation code an “inlet” in the ground, to reproduce a vent from which the particles are generated. To obtain the velocity of these particles, we need to divide the effusion rate for a reference area. To obtain this quantity, we calculated a maximum value of TADR, averaging the maximum values of each eruption obtained from satellite and shown in Table 1, and considered also an averaged lava exit speed (taking inspiration from studies on strombolian activity (Pioli et al., 2022)). The TADR obtained clearly does not correspond to lava volume value over time emitted by the vent during a lava fountain, but it can be considered as an averaged peak value scaled with respect to the data type used (satellite observations). We then calculated the dimensions of a fictitious vent (i.e., the diameter of the vent, that here results as a line in the 2D simulations, considered thus as the total vent area) such as to satisfy the fixed TADR and exit speed values that are expected to be achieved for the

cases analyzed using these fixed values. The obtained fictitious vent area is used in the vent (inlet) exit particles velocity calculation. In contrast, the real vent (2D) dimension of the simulations is set to be equal to 20 m for each case study. Finally, we added all this information to the numerical code and started the simulation.

3.2 Second step: numerical simulations with SPH discretization

We apply a Computational Fluid Dynamics (CFD) model to reproduce the fluid behavior, applying the results obtained in the first step from real satellite data analysis to the numerical model. We consider as CFD reference model the Smoothed Particle Hydrodynamics (SPH), a particle-based Lagrangian mesh-free method, that uses smoothing kernels to discretize the spatial derivatives of the governing fluid dynamics equations (Monaghan, 1992, 2005). It is largely used for complex fluids simulations, with solid-fluid interactions and free-surface flows simulations, catching well the kinematic and viscous and thermal details of the fluid (Zago et al., 2017, 2021). SPH has been already largely used in lava flows simulations due to the reliability in complex physics simulation and for being highly parallelizable (executable on GPUs – Graphics Processing Units), with different formulations (Bilotta et al., 2016, 2022; Hérault et al., 2011; Zago, Bilotta, Hérault, et al., 2018).

We model the fluid according to the governing fluid dynamics equations. The following Eq. (4) is the continuity equation (law of conservation of mass), the Eq. (5) is the Navier-Stokes equation (law of conservation of momentum, for incompressible fluids, viscous case), and the Eq. (6) is the heat equation,

$$\frac{D\rho}{Dt} = -\rho\nabla\cdot\boldsymbol{u} \tag{4}$$

$$\rho\frac{D\boldsymbol{u}}{Dt} = -\nabla P + \nabla\cdot(\mu\nabla\boldsymbol{u}) + \boldsymbol{g} \tag{5}$$

$$\frac{DT}{Dt} = \frac{1}{c_p\rho}\nabla(\kappa\nabla T) \tag{6}$$

with ρ the density, $\boldsymbol{u}$ the velocity, P the pressure, μ the dynamic viscosity, and $\boldsymbol{g}$ the external forces (e.g., here the gravity). T is the temperature, c_p the specific heat at constant pressure, and κ the thermal conductivity, D/Dt the total derivative with respect to time.

Following the 2D SPH formulation of (Zago, Bilotta, Hérault, et al., 2018), the equation of the mass conservation is discretized as in Eq. (7), the equation of momentum conservation (viscous case) as in Eq. (8), and the heat equation as in Eq. (9).

$$\frac{D\rho_i}{Dt} = -\sum_j \boldsymbol{u}_{ij}\boldsymbol{x}_{ij}F_{ij}m_j + \xi h c_0 \sum_j \boldsymbol{\psi}_{ij}F_{ij}m_j \tag{7}$$

$$\frac{D\boldsymbol{u}_i}{Dt} = \sum_j \left(\frac{P_i}{\rho_i^2} + \frac{P_j}{\rho_j^2}\right) F_{ij}m_j\,\boldsymbol{x}_{ij} - \sum_j \frac{2\boldsymbol{\mu_{ij}}}{\rho_i\rho_j}F_{ij}m_j\boldsymbol{u}_{ij} + \boldsymbol{g} \tag{8}$$

$$\frac{DT_i}{Dt} = -\frac{1}{c_p\rho_i}\sum_j \frac{2m_j\kappa T_{ij}}{\rho_j}F_{ij} \tag{9}$$

We use a fifth order Wendland smoothing kernel W (Wendland, 1995), for which $\mathrm{F(r)} = \frac{1}{\mathrm{r}}\frac{\partial \mathrm{W}}{\partial \mathrm{r}}$, with $r = |\mathbf{x}_{ij}|$ the distance, then $F_{ij} = F(r)$, and $\nabla_j W_{ij} = -\mathbf{x}_{ij}F_{ij}$. In the Eq. (7), $\boldsymbol{\psi}_{ij}$ is the density diffusion (typically with $\xi = 0.1$

density diffusion coefficient) (Antuono et al., 2012), defined as $\boldsymbol{\psi}_{ij} = 2\left(\frac{\rho_j}{\rho_i} - 1\right)$ if $\frac{|P_i - P_j|}{\rho_i \boldsymbol{g}|\boldsymbol{y_i} - \boldsymbol{y_j}|} > 1, \boldsymbol{\psi}_{ij} = 0$ otherwise. In Eqs. (7-9), the parameters are defined as h the smoothing length, m the mass, $\boldsymbol{x}$ the position, c_0 the speed of sound (calculated at density ρ_0 at rest, and defined 10 times higher than the maximum velocity that can be achieved in the simulation). All these parameters can be followed by the symbol i or j as a subscript to indicate the relative particle considered, or ij to indicate that the parameter under consideration is calculated in relation to two particles (i and j particles).

The pressure P, in Eq. (10), is derived from the density using a state equation (Cole and Weller, 1948):

$$P(\rho) = c_0^2 \frac{\rho_0}{\gamma}\left(\left(\frac{\rho}{\rho_0}\right)^{\gamma} - 1\right) \tag{10}$$

with ρ_0 the density at rest, c_0 the speed of sound (at ρ_0) defined 10 times higher than the maximum velocity reachable in the simulation, according to the formulation of Weak Compressibility condition (to maintain the speed of sound large enough to bound density variations within certain ranges) (Monaghan, 2005; Monaghan and Kos, 1999). γ is the polytropic constant.

The spatial resolution is set as $\Delta p = 0.75$ m (used for cases of time-independent effusive rate). Due to the limitations of the SPH method in conducting simulations that are expensive in terms of time and resources and with respect to the computing power available, in the case of time-dependent effusion rate it is necessary to lower the spatial resolution of the simulation, without loss of information, using $\Delta p = 3.0$ m.

Once the spatial derivatives have been evaluated and discretized, the Partial Differential Equations (PDEs) (Eqs. 4-6) are reduced to Ordinary Differential Equations (ODEs) with derivatives over time (Eqs. 7-9). We used a predictor-corrector integration scheme to integrate these equations (Zago et al., 2021), with time-step calculated as $\Delta t = min_i \Delta t_i$, with Δt_i to fulfill CFL-like (Courant-Friedrichs-Lewy) stability conditions (Eq. 11) (Monaghan, 1992),

$$\Delta t_i \leq min\left\{0.3\sqrt{\frac{h}{\|\boldsymbol{a}_i\|}},\ 0.3\frac{h}{c_0},\ 0.125\frac{\rho_0 h^2}{\mu_i},\ 0.1\frac{\rho_0 c_p h^2}{\kappa}\right\} \tag{11}$$

with a_i the acceleration of the particle i.

The model is implemented in Python using double precision variables and it is run on CPU (Saikali et al., 2020).

Some kinds of fluids (as lava or oil) have a peculiar behavior, which links viscosity and temperature (as temperature increases, viscosity decreases, and vice versa). Therefore, we calculated the temperature-dependent viscosity using a power law relationship (Eq. 12) (Amato, 2024; Cordonnier et al., 2016; Hérault et al., 2011), with c a constant of proportionality (Amato, 2024), and we used it into the momentum conservation equation.

$$\mu_i(T_i) = ce^{\frac{1}{T_i}} \tag{12}$$

Moving to more physical meaning, we also numerically added the phase transition, defining a parameter q (with $0 \leq q \leq 1$) that describes the fraction of latent heat gained/lost during the transition (Hérault et al., 2011; Zago, 2018). $q = 1$ indicates solid particles and $q = 0$ liquid particles. For particles not involved in the phase transition (with $q = 1$ or $q = 0$), temperature evolves normally following the discretized heat equation (Hérault et al., 2011; Zago, 2018). For fluid particles ($q = 0$), when temperature reaches solidification temperature, using $T_{solidus} = 1150$ K, temperature is fixed at $T_{solidus}$ and we update the q with the quantity $\Delta q = c_p(T_{solidus} - T_i)/L$, with latent heat $L = 3.3 \times 10^5$ J/kg (Cordonnier et al., 2016; Hérault et al., 2011). The particle state changes when the fraction of latent heat moves from $q = 0$ (liquid particles) to $q = 1$ (solid particles) and temperature resumes evolving according to the discretized heat equation.

Finally, we recognize the free surface particles through a neighbor count (based on the smoothing kernel that is used to compute the particles interactions), to detect the boundary particles on which to apply the surface effects. As boundary conditions we use the dynamic boundary model (Bilotta et al., 2022). Once surface particles were

detected, we applied thermal radiation and air convection functions over them (Zago, Bilotta, Cappello, et al., 2018). The contribution for thermal radiation is calculated as in Eq. (13), following the Stefan-Boltzmann law, with K_B the Stefan-Boltzmann constant, ϵ the emissivity, m the mass and T_{env} the environmental temperature.

$$\frac{DT_i}{Dt} = -\frac{K_B \kappa \epsilon}{m_i c_p}\left(T_i{}^4 - T_{env}^4\right) \tag{13}$$

The contribution of air convection (Eq. 14) is not calculated directly modeling the air particles but computing the heat lost by the fluid surface with a convection coefficient η

$$\frac{DT_i}{Dt} = -\frac{\eta}{m_i c_p}(T_i - T_{env}) \tag{14}$$

These two contributions are added to the temperature derivative obtained from the heat equation (Eq. 9).

The interaction of the particles that discretize the fluid with the neighboring ones modifies the state of each particle, following the fluid dynamics laws discretized with the SPH method.

For the simulation domain, we have used a topography with bumps, to simulate a volcano flank, preceded by a plateau, to simulate the crater. We also added an inlet with a (2D) dimension of 20 m to simulate the vent from which the particles are generated, with a velocity sufficient to satisfy the law for the effusive rate. We simulated a fluid similar to lava, using the simulation parameters in Table 2, that are comparable to parameters in (Cordonnier et al., 2016; Hérault et al., 2011).

Applying all these equations, the homogeneously step-by-step generated fluid presents the same characteristics, i.e., same density, temperature, and viscosity at the vent. These vent conditions are constant in time. This is not

Parameter	Value	Unit of measurement
ρ_0	2400	kg/m^3
c_0	2500	m/s
γ	7	—
T_{inlet}	1350	K
T_{env}	290	K
c_p	1100	J/(kg K)
κ	2	W/(m K)
K_B	$5.67037442 \times 10^{-8}$	kg/(s^3 K^4)
ϵ	0.96	—
η	20	W/(m^2 K)

Table 2. Values of the simulation parameters for the *lava-like* model (comparable to (Cordonnier et al., 2016; Hérault et al., 2011)).

a realistic assumption, but it can be applied to reach our first aim to analyze the effects of different effusion rates on the fluid flow. Future developments will incorporate additional volcanic parameters, such as gas emissions and different magma viscosity exit values, to determine the eruption dynamics.

Discussing the effusion rate parameter, we consider three case studies in which its values were modified: two constant values for the effusion rate and a time-dependent formulation from Eq. (3), obtained from satellite data. Firstly, the effusion rate is constantly set equal to 3 m^3/s, one of the lower effusion rate values for the 15 July 2024 Mt. Etna eruption satellite observations. Secondly, it is constantly set equal to 21.17 m^3/s, i.e., obtained averaging the maximum TADR satellite values in Table 1. Finally, the time-dependent effusion rate is set following the final averaged effusion rate formula for the July-August 2024 Mt. Etna TADR values (with the functional form in Eq. 3).

4. Results

We apply the two-step approach to the July-August Mt. Etna activity at the Voragine crater (Fig. 1).

Firstly, we present an example of the procedure used for each eruption, focusing on the eruption of 15 July 2024. Figure 2 shows in the left y-axis the VRP (in MW), starting from 15 July 2024 05:12 UTC and ending on 17 July 2024 08:42 UTC. We applied the Eqs. (1-2) to convert the VRP values (that must be previously converted in watt) of the Mt. Etna eruption of 15 July 2024 in TADR values (Fig. 2 right y-axis, in m^3/s).

Using the Lorentzian curve in Eq. (3), we fitted the relative parameters: A amplitude, w width, and c center. In Fig. 2, the green curve shows an example of the fitting curve for the TADR data related to the 15 July 2024 eruption, with parameters A = 3.463, w = 3.574, and c = 17.313.

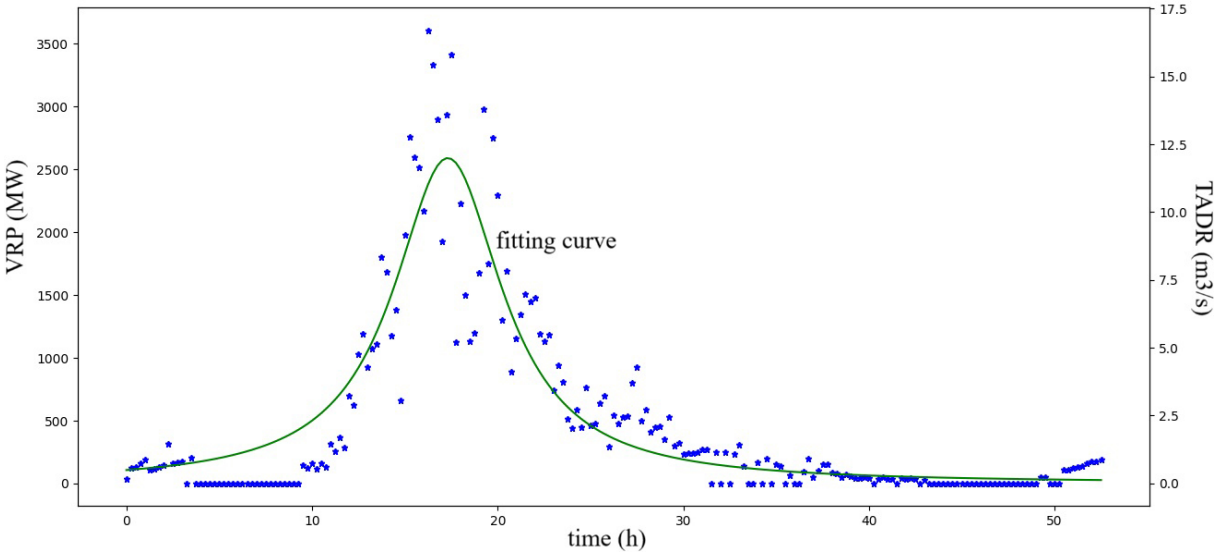

Figure 2. VRP (MW) (left y-axis) and TADR (m^3/s) (right y-axis) over time (in hours, x-axis) for the 15 July 2024 Mt. Etna eruption, with relative Lorentzian fitting curve (in green) for TADR data, with parameters A = 3.463 (amplitude), w = 3.574 (width), and c = 17.313 (center).

We also calculated the R^2 coefficient of determination (James et al., 2013), as in Eq. (15), to evaluate the goodness of the fitting (the proportion of variability in TADR values that can be explained using time t in the $f(t)$ fitting curve estimated, $0 \leq R^2 \leq 1$, $R^2 = 0$ for bad match, $R^2 = 1$ for perfect match), obtaining a value of $R^2 = 0.83$ that indicates a good representation of the data by the $f(t)$ fitting curve,

$$R^2 = 1 - \frac{\sum_{t=1}^{n}(TADR(t) - TADR_{est}(t))^2}{\sum_{t=1}^{n}(TADR(t) - \overline{TADR}(t))^2} \quad (15)$$

In Eq. (15), $TADR$ indicates the satellite TADR values, $TADR_{est}$ the estimated TADR (using the fitting curve in Eq. 3), and $\overline{TADR}$ the average of the satellite TADR values, with each value considered for each time-step (i.e., for each observation, with n total number of observations).

We have reported in Table 3 all the fitting parameters estimated with this method and the relative R^2 coefficients, for each of the analyzed eruptions.

Eruption date	A	w	c	R^2
04-05 July 2024	3.466	3.657	76.835	0.68
07 July 2024	4.184	1.995	5.494	0.92
15 July 2024	3.463	3.574	17.313	0.83
22-23 July 2024	2.861	4.323	12.493	0.80
04 August 2024	4.004	2.195	12.267	0.78
14-15 August 2024	2.541	4.860	16.918	0.67

Table 3. Fitting parameters for the analyzed eruptions.

As shown by the data in Table 3, similar patterns in the fitting trends can be observed, specifically in A and w parameters. By combining all these curves, we can obtain a single averaged trend that represents the behavior of this eruptive phase at Mt. Etna. Thus, we calculated the mean values for A amplitude, w width, and c center, to reproduce an average eruptive style. The final averaged curve for the TADR values in time (hours) has the formulation in Eq. (3), with averaged fitted parameters $A = 3.420$, $w = 3.434$, $c = 23.553$, thus obtaining the Eq. (16). These values are scaled with respect to the data type used to obtain it, that are satellite observations, but in a very good way they follow the trend of the volcanic eruptions (so, they are qualitatively realistic). We finally convert time in seconds to use this formula in the simulations.

$$f(t) = \frac{3.420^2\ 3.434^2}{(t - 23.553)^2 + 3.434^2} \tag{16}$$

To determine the exit velocity (vertical component) of particles generated from the vent (referred to as the "inlet"), we first calculated the maximum value of TADR, by averaging the peak values of each eruption shown in Table 1, obtaining a final maximum TADR of 21.17 m^3/s. Again, it is worth to clarify that the TADR value obtained does not correspond to a real lava volume value over time emitted by the vent during the eruption, but it can be considered as an indicative average peak value scaled and in accordance with the satellite data used. We also considered an averaged lava particles exit speed of 200 m/s (taking inspiration from studies on strombolian activity (Pioli et al., 2022)) and calculated the dimensions of a fictitious vent that would satisfy the fixed TADR and exit speed values expected during the eruptive activity (i.e., a 2D dimension of the fictitious vent of 0.37 m; it should be an area but it is considered in a 2D simulation, so as if it were a linear length). This fictitious vent dimension is then used in the vent (inlet) exit particles velocity calculation. However, the actual vent used in the simulation is fixed at 20 m for each case study. We applied the same effusion rate and velocity values calculated in this manner for each particle generated from the inlet.

Another assumption is made, linked to the computing power availability. Considering the limitations of the SPH method in conducting expensive simulations in terms of time and resources, in the case of time-dependent

effusion rate, in which a longer simulation time is needed to see more clearly the effects of the time-dependent effusive rate (with consequent high computational costs, due to the significant increase in the number of particles to be simulated), we lowered the spatial resolution of the simulation. Therefore, we used a spatial resolution of $\Delta p = 0.75$ m, in cases of time-independent effusive rate, and change it to $\Delta p = 3.0$ m, for the time-dependent effusive rate cases, to allow the simulation to be carried out in reasonable time. The resolution changes do not affect the simulation behavior, as it is possible to verify in Fig. 5, in which we show the first seconds of fluid simulation with time-dependent effusion rate, comparing the higher resolution ($\Delta p = 0.75$ m, in magenta), with the lower resolution ($\Delta p = 3.00$ m, in yellow). Except for some numerical instabilities and some more detailed fluid characteristics that arise with high resolutions, the general trend of the two simulations is perfectly in agreement, therefore it is permissible to lower the resolution to computationally lighten the simulation, without an excessive loss of information.

Subsequently, following the second step of the approach discussed, we applied the results obtained from real satellite data analysis to the numerical model, to simulate lava flows, comparing the three effusion rate case studies obtained from real data, that are the constant values of 3 m^3/s and 21.17 m^3/s, and the time-dependent effusion rate as in Eq. (3), obtained with the averaged curve.

Figures 3, 4, and 6 show the simulations of fluids with temperature-dependent viscosity (using the power law for visco-thermal coupling), with fluid temperature of 1350.0 K and boundaries temperature of 290.0 K.

In Fig. 3 the effusion rate is constantly set equal to 3 m^3/s, and we consider the times t = 5.0 s (Fig. 3a), t = 10.0 s (Fig. 3b), t = 20.0 s (Fig. 3c), and t = 35.0 s (Fig. 3d). The relatively low value of the effusive rate causes the flow to evolve in a controlled way, maintaining an effusive/explosive-Strombolian like activity with overflows.

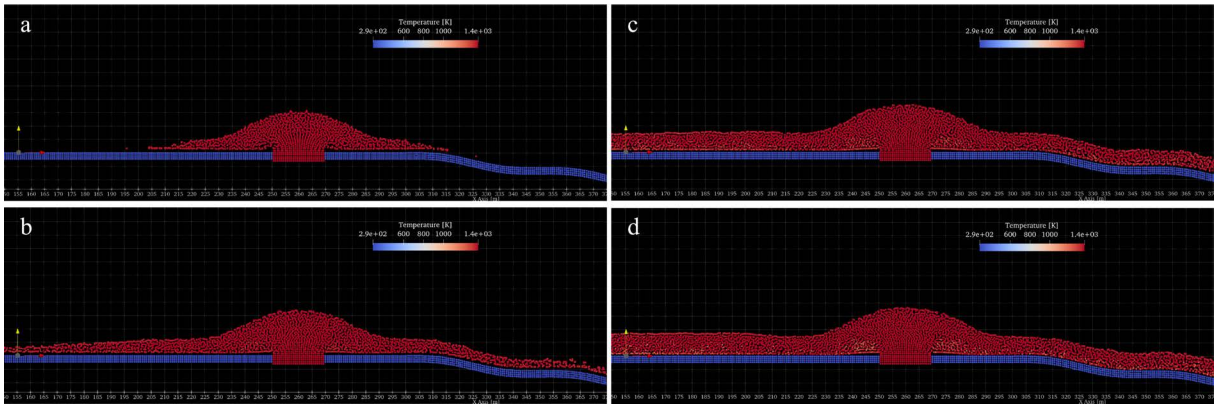

Figure 3. Simulation of fluid with temperature-dependent viscosity, fluid temperature 1350.0 K, boundaries temperature 290.0 K, and constant effusion rate (equal to 3 m^3/s). Spatial resolution $\Delta p = 0.75$ m. Time (a) t = 5.0 s, (b) t = 10.0 s, (c) t = 20.0 s, (d) t = 35.0 s. Particles are colored by Temperature (K).

Figure 4 shows the fluid simulation with effusion rate constantly set equal to 21.17 m^3/s. We report results at times t = 1.0 s (Fig. 4a), t = 5.0 s (Fig. 4b), t = 10.0 s (Fig. 4c), t = 17.0 s (Fig. 4d). We zoomed out the figures respect to the other cases (to see approximatively double the domain height) because the high value of the effusive rate causes the fluid flow to rapidly evolve, reaching sustained jets already from the first seconds, followed by overflows.

Moving to the case of fluid simulation with the time-dependent effusion rate as in Eq. (16), obtained with the averaged fitting curve, due to the high computational costs of the simulation, we lowered the spatial resolution of the simulation, moving it from $\Delta p = 0.75$ m (used for cases of time-independent effusive rate) to $\Delta p = 3.0$ m, to allow the simulations to be carried out in reasonable time. Figure 5 shows a comparison between the fluid simulation with time-dependent effusion rate and the higher resolution ($\Delta p = 0.75$ m, in magenta), and the same simulation with the lower resolution ($\Delta p = 3.00$ m, in yellow), for two different times. The general trend of the two simulations is perfectly in agreement (except for some numerical instabilities and some more detailed fluid characteristics in the high-resolution case), making possible to lower the resolution without loss of information.

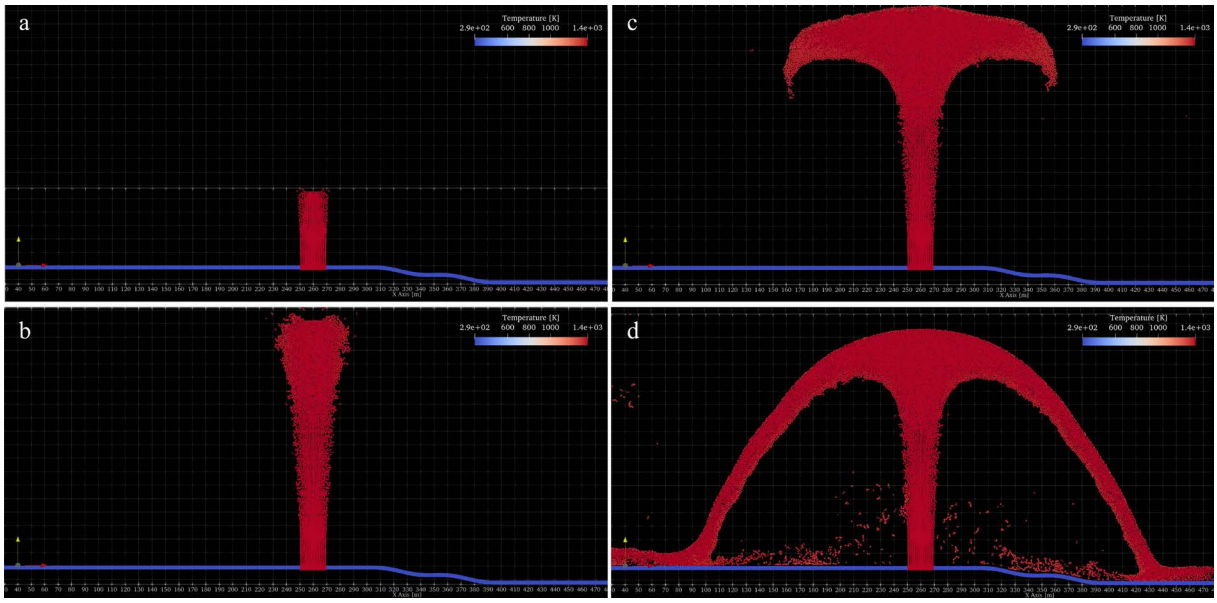

Figure 4. Simulation of fluid with temperature-dependent viscosity, fluid temperature 1350.0 K, boundaries temperature 290.0 K, and constant effusion rate (equal to 21.17 m^3/s). Spatial resolution $\Delta p = 0.75$ m. Time (a) t = 1.0 s, (b) t = 5.0 s, (c) t = 10.0 s, (d) t = 17.0 s (zoomed out respect to the other figures to see double the domain height). Particles are colored by Temperature (K).

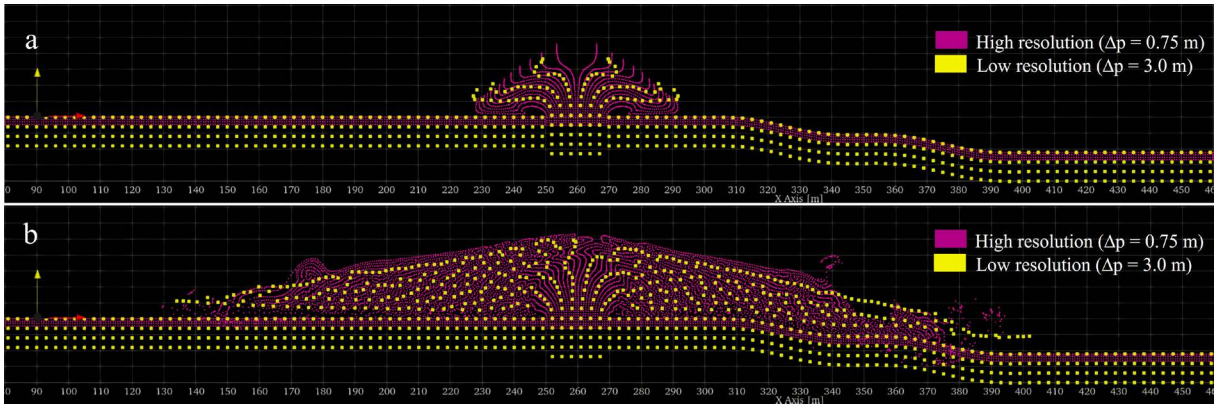

Figure 5. Comparison between the fluid simulation with time-dependent effusion rate and the higher resolution ($\Delta p = 0.75$ m, in magenta), and the same simulation with the lower resolution ($\Delta p = 3.00$ m, in yellow). Time (a) t = 60.0 s, (b) t = 360.0 s.

Figure 6 shows the fluid simulation with the time-dependent effusion rate (as in Eq. 16). We report the results at times t = 180.0 s (Fig. 6a), t = 540.0 s (Fig. 6b), t = 750.0 s (Fig. 6c), t = 1050.0 s (Fig. 6d). Already these first times can show the flow evolution, with a precursory activity mainly effusive/Strombolian with overflows, that will evolve in sustained jets and a waning final phase (it becomes computationally too expensive to proceed much further in the simulation time with these parameters setting).

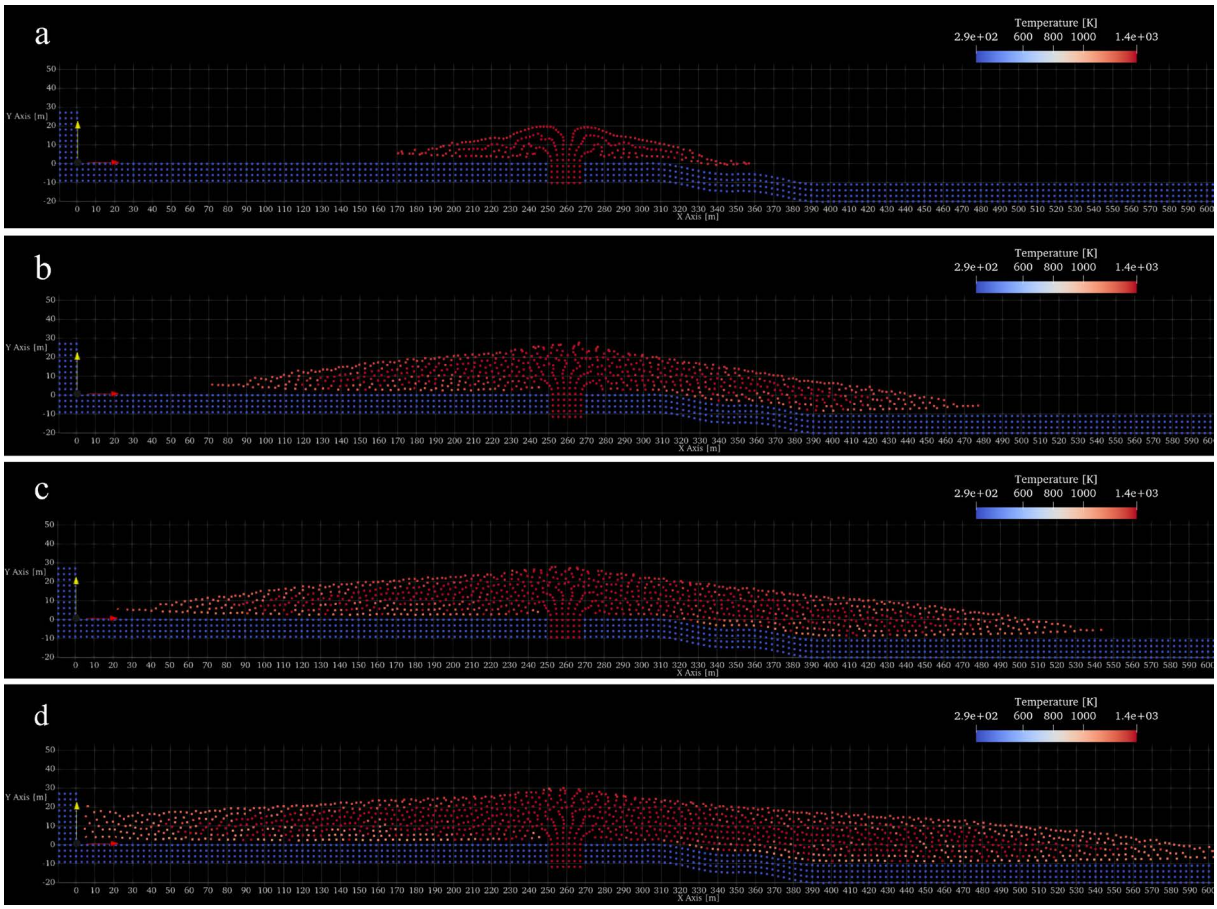

Figure 6. Simulation of fluid with temperature-dependent viscosity, fluid temperature 1350.0 K, boundaries temperature 290.0 K, and time-dependent effusion rate (obtained by the averaged fitting curve, as in Eq. 16). Spatial resolution $\Delta p = 3.0$ m. Time (a) t = 180.0 s, (b) t = 540.0 s, (c) t = 750.0 s, (d) t = 1050.0 s. Particles are colored by Temperature (K).

To overcome the difficulties related to the impossibility of proceeding too far with the simulation, a small modification in the parameters used in the function for the effusive rate (Eq. 3) can be applied. It is interesting to note that the parameter c of the function in Eq. (3) is related to the "center" of the fitted function, which physically describes the peak of the TADR (and VRP) value, typically approximately coincident with the peak of the fountaining activity, in optimal weather conditions. In Eq. (16) we used the estimated value $c = 23.553$, obtained averaging this parameter for the different Mt. Etna eruption under analysis. Given its physical meaning, it is possible to modify the value of the c parameter, reducing it to model a volcanic event that reaches its peak earlier in time, so as to be able to observe such eruptive behavior earlier in the numerical simulation. We have therefore brought this value to $c = 3.0$. Figure 7 reports the progress of a new simulation with the same physical parameters as the previous one, except for this parameter (here $c = 3.0$), at time t = 30.0 s (Fig. 7a), t = 60.0 s (Fig. 7b), t = 180.0 s (Fig. 7c), t = 1410.0 s (Fig. 7d), showing a similar behavior of the simulation in Fig. 6, but with a flow that rapidly evolves in a sustained jet with overflows, which will then be followed by a waning final phase.

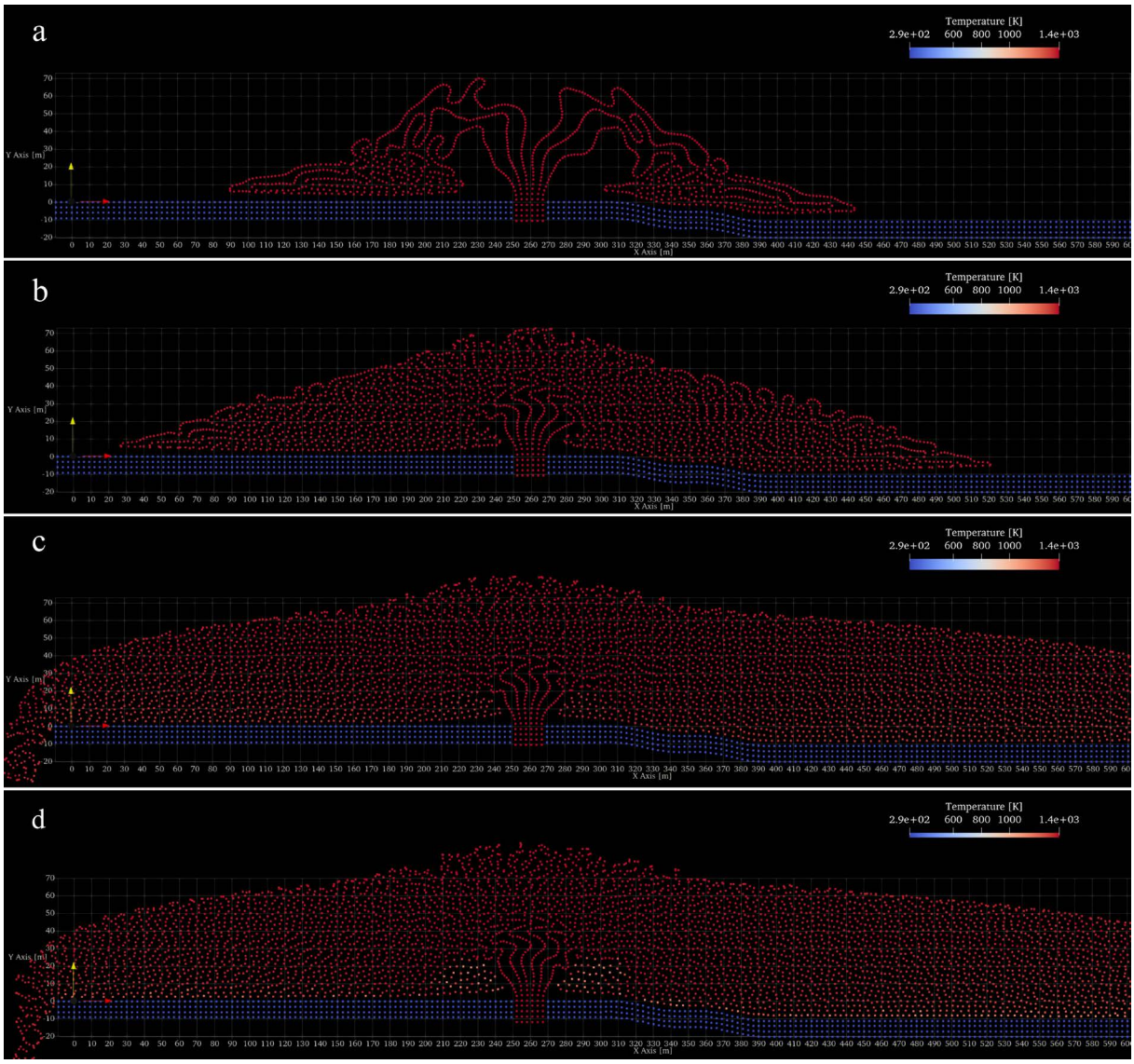

Figure 7. Simulation of fluid with temperature-dependent viscosity, fluid temperature 1350.0 K, boundaries temperature 290.0 K, and time-dependent effusion rate (obtained by the averaged fitting curve, as in Eq. 16, but with parameter $c = 3.0$ here). Spatial resolution $\Delta p = 3.0$ m. Time (a) t = 30.0 s, (b) t = 60.0 s, (c) t = 180.0 s, (d) t = 1410.0 s. Particles are colored by Temperature (K).

5. Discussion

The results of this study highlight the critical role of effusion rate in shaping volcanic eruption styles and determining the behavior of lava flows. The numerical simulations conducted, based on satellite-derived Volcanic Radiative Power (VRP) and Time Averaged Discharge Rate (TADR), have shown that even subtle changes in effusion rate can result in dramatically different volcanic behaviors. For instance, lower effusion rates often result in slow-moving flows associated with effusive or Strombolian activity (Fig. 3), while higher effusion rates lead to explosive activity, with a fluid flow that rapidly evolves in a sustained jet (Fig. 4), as shown by our simulations. Moreover, a time-dependent effusion rate results in a variable flow, starting from effusive/Strombolian activity that will evolve into sustained jets and overflows, which will then be followed by a waning phase, that lasts until the end of the simulation (Figs. 6-7).

In previous studies, the importance of effusion rates has been widely acknowledged in modeling volcanic eruptions. Research by (Coppola et al., 2012; Harris, 2013) has already underscored that effusion rate affects key volcanic parameters such as flow length, thickness, and the overall dynamics of lava emplacement. Our study builds

on this foundation by focusing on the sensitivity of 2D numerical models to changes in effusion rate. Specifically, the use of a Smoothed Particle Hydrodynamics (SPH) model allowed us to simulate both the horizontal flow front evolution and its vertical cross-sections. This dual focus provided valuable insights into how effusion rate modulates not only the surface extent of lava flows but also their internal structures.

Some limitation is present; the TADR value obtained must be considered as an average peak value scaled and in accordance with the (numerous, easily accessible, safe) satellite data used. In addition, the limitations of the SPH method in conducting expensive simulations in terms of time and resources, in the case of time-dependent effusion rate, have forced us to lower the spatial resolution of the simulations, to allow the simulations to be carried out in reasonable time. Despite these limitations, and a qualitative study of the events, this work demonstrates the quality of simulations when varying the effusive rate, and how this parameter impacts on them.

Several key points arise from our results. Firstly, our simulations showed that higher effusion rates produce more rapid and expansive flows, as seen in the simulations with effusion rates of 21.17 m^3/s (Fig. 4). These findings align with previous works by (Wadge, 1981), who showed that higher discharge rates are associated with longer flow lengths and more sustained lava fountains. In contrast, simulations with lower effusion rates, such as 3 m^3/s (Fig. 3), resulted in limited flow advance and more confined fluid emplacement, consistent with more effusive activity. Finally, time-dependent effusion rate affects the fluid simulations (Figs. 6-7), obtaining a general eruptive behavior with a precursory activity mainly effusive/Strombolian, that evolves in sustained jets, with a waning final phase.

6. Conclusions

The use of real satellite data (VRP and TADR) in combination with CFD numerical models (SPH method) represents an advancement in modeling volcanic eruptions. The integration of these observations (numerous, easily accessible, safe) into numerical models not only enhances the accuracy of predictions but also provides a framework for future applications. For example, the analytical formulation of effusion rates derived from satellite VRP data offers a pathway for simulating ongoing eruptions in real-time, allowing for dynamic hazard assessment without dangers linked to direct observations. This type of "data fusion" approach – combining numerical modeling with real-time observations – could significantly improve the ability to forecast volcanic hazards and the mitigation strategies.

We have thus here presented a framework to simulate lava flows with different physical parameters, conducting a sensitivity analysis on the qualitative effects of effusion rate in 2D numerical modeling and bringing to a deeper knowledge of the different eruptive behaviors in function of this parameter.

Future directions for research include refining the SPH model by incorporating additional volcanic parameters, such as gas emissions and concentrations, and magma viscosity exact values, which also play a critical role in determining eruption dynamics.

Furthermore, the use of Artificial Intelligence (AI) algorithms in conjunction with traditional numerical models, as suggested by (Amato et al., 2024), offers exciting potential for developing AI-based *emulators* of volcanic systems, speeding-up the simulations and enhancing their performance. In detail, these AI-enhanced models could not only speed-up computational processes but also provide more accurate, real-time simulations of volcanic events (Amato, 2024; Amato et al., 2024; Bortnik and Camporeale, 2021). In addition, the AI-based emulators could also be seen as Digital Twins of natural phenomena (Kapteyn and Willcox, 2020), making possible to faithful reproduce and study natural events. Moreover, the combination with Quantum Computing, as in Bazgir and Zhang (2024), can also offer better predictive performance in Earth modeling, improving accuracy and efficiency of the simulations. For these reasons, future developments will also consider the effect of effusion rate in these advanced models, verifying their capability to also reproduce this time-dependent volcanic parameter.

In conclusion, our approach highlights how the effusion rate can affect the lava flow simulations, demonstrating the importance of this parameter in dictating eruption styles and lava flow behavior. The integration of real observational data with numerical models represents a significant step forward in volcanic hazard assessment. As we continue to refine these models and integrate AI technologies, the potential for more accurate and timely predictions of volcanic activity will only grow, providing valuable tools for scientists and policymakers alike.

Data availability statement. Data are available from the corresponding author upon reasonable request.

Acknowledgements. This work was developed within the framework of the Laboratory of Technologies for Volcanology (TechnoLab) at the Istituto Nazionale di Geofisica e Vulcanologia (INGV) in Catania (Italy). This research was funded by the ATHOS Research Program (INGV OB.FU. 0867.010), by the 2019 Strategic Project FIRST – ForecastIng eRuptive activity at Stromboli volcano: timing, eruptive style, size, intensity, and duration – of the INGV Volcanoes Department (Delibera n. 144/2020), and by Project INGV Pianeta Dinamico VT_ORME 2023-2025 (INGV OB.FU. 1020.010).

References

Alberico, I., L. Lirer, P. Petrosino and R. Scandone (2002). A methodology for the evaluation of long-term volcanic risk from pyroclastic flows in Campi Flegrei (Italy), J. Volcanol. Geoth. Res., 116, 1-2, 63-78, doi:10.1016/S0377-0273(02)00211-1.

Amadio, F., L. Pioli and S. Scollo (2024). Constraining proximal grainsize distribution of tephra from paroxysmal eruptions at Etna volcano, J. Volcanol. Geoth. Res., 454, 108164. doi:10.1016/j.jvolgeores.2024.108164.

Amato, E. (2022). Machine learning and best fit approach to map lava flows from space, Il Nuovo Cimento C, 45, 4, 1-12. doi:10.1393/ncc/i2022-22080-1.

Amato, E. (2024). Enhancing Computational Fluid Dynamics with Artificial Intelligence: an AI-based Smoothed Particle Hydrodynamics (SPH) Emulator for Lava Flow Modeling (Ph.D. Thesis, Università degli Studi di Palermo), https://hdl.handle.net/20.500.14242/172361.

Amato, E., C. Corradino, F. Torrisi and C. Del Negro (2023a). A Deep Convolutional Neural Network for Detecting Volcanic Thermal Anomalies from Satellite Images. Remote Sens., 15, 15, 3718, doi:10.3390/rs15153718.

Amato, E., C. Corradino, F. Torrisi and C. Del Negro (2023b). Spectral analysis of lava flows: Temporal and physicochemical effects, Il Nuovo Cimento C, 46, 5, 1-4, doi:10.1393/ncc/i2023-23144-4.

Amato, E., C. Corradino, F. Torrisi and C. Del Negro (2021). Mapping lava flows at Etna Volcano using Google Earth Engine, open-access satellite data, and machine learning. 2021 International Conference on Electrical, Computer, Communications and Mechatronics Engineering (ICECCME), 1-6, doi:10.1109/ICECCME52200.2021.9591110.

Amato, E., V. Zago and C. Del Negro (2024). A physically consistent AI-based SPH emulator for computational fluid dynamics, Nonlinear Engineering, 13, 1, 20220359, doi:10.1515/nleng-2022-0359.

Antuono, M., A. Colagrossi and S. Marrone (2012). Numerical diffusive terms in weakly-compressible SPH schemes, Comput. Phys. Commun., 183, 12, 2570-2580, doi:10.1016/j.cpc.2012.07.006.

Aravena, A., R. Cioni, D. Coppola, M. De' Michieli Vitturi et al. (2020). Effusion Rate Evolution During Small-Volume Basaltic Eruptions: Insights From Numerical Modeling, J. Geophys. Res.-Solid Earth, 125, 6, e2019JB019301, doi:10.1029/2019JB019301.

Aravena, A., R. Cioni, M. De' Michieli Vitturi, M. Pistolesi et al. (2018). Evolution of Conduit Geometry and Eruptive Parameters During Effusive Events, Geophys. Res. Lett., 45, 15, 7471-7480, doi:10.1029/2018GL077806.

Bazgir, A. and Y. Zhang (2024). QESM: A Leap Towards Quantum-Enhanced ML Emulation Framework for Earth and Climate Modeling (arXiv:2410.01551). arXiv, doi:10.48550/arXiv.2410.01551.

Bilotta, G., A. Cappello, A. Hérault, A. Vicari et al. (2012). Sensitivity analysis of the MAGFLOW Cellular Automaton model for lava flow simulation. Environ Model Softw, 35, 122-131. doi:10.1016/j.envsoft.2012.02.015.

Bilotta, G., A. Hérault, A. Cappello, G. Ganci et al. (2016). GPUSPH: a Smoothed Particle Hydrodynamics model for the thermal and rheological evolution of lava flows, Geological Society, London, Special Publications, 426, 1, 387-408, doi:10.1144/SP426.24.

Bilotta, G., V. Zago, V. Centorrino, R. A. Dalrymple et al. (2022). A numerically robust, parallel-friendly variant of BiCGSTAB for the semi-implicit integration of the viscous term in Smoothed Particle Hydrodynamics, J. Comp. Phys., 466, 111413, doi:10.1016/j.jcp.2022.111413.

Bortnik, J. and E. Camporeale (2021). Ten Ways to Apply Machine Learning in Earth and Space Sciences, Eos, 102, doi:10.1029/2021EO160257.

Calvari, S., F. Di Traglia, G. Ganci, F. Giudicepietro et al. (2020). Overflows and Pyroclastic Density Currents in March-April 2020 at Stromboli Volcano Detected by Remote Sensing and Seismic Monitoring Data, Remote Sens., 12, 18, 3010, doi:10.3390/rs12183010.

Calvari, S. and G. Nunnari (2024). Reawakening of Voragine, the Oldest of Etna's Summit Craters: Insights from a Recurrent Episodic Eruptive Behavior, Remote Sens., 16, 22, 4278, doi:10.3390/rs16224278.

Calvari, S. and H. Pinkerton (1998). Formation of lava tubes and extensive flow field during the 1991-1993 eruption of Mount Etna, J. Geophys. Res.: Solid Earth, 103, B11, 27291-27301, doi:10.1029/97JB03388.

Cappello, A., G. Bilotta, M. Neri and C. Del Negro (2013). Probabilistic modeling of future volcanic eruptions at Mount Etna, J. Geophys. Res: Solid Earth, 118, 5, 1925-1935, doi:10.1002/jgrb.50190.

Cappello, A., G. Ganci, G. Bilotta, A. Herault et al. (2018). Satellite-driven modeling approach for monitoring lava flow hazards during the 2017 Etna eruption, Ann Geophys-Italy, 61, 1, doi:10.4401/ag-7792.

Cioni, R., D. Andronico, L. Cappelli, A. Aravena et al. (2023). Products and dynamics of lava-snow explosions: The 16 March 2017 explosion at Mount Etna, Italy, Geol. Soc. Am. Bull., doi:10.1130/B37102.1.

Cole, R. H. and R. Weller (1948). Underwater Explosions, Phys Today, 1, 6, 35-35, doi:10.1063/1.3066176.

Coppola, D., A. Di Muro, A. Peltier, N. Villeneuve et al. (2017). Shallow system rejuvenation and magma discharge trends at Piton de la Fournaise volcano (La Réunion Island). Earth Planet. Sci.Lett., 463, 13-24, doi:10.1016/j.epsl.2017.01.024.

Coppola, D., M. Laiolo, D. Piscopo and C. Cigolini (2013). Rheological control on the radiant density of active lava flows and domes, J. Volcanol. Geoth. Res., 249, 39-48, doi:10.1016/j.jvolgeores.2012.09.005.

Coppola, D., D. Piscopo, M. Laiolo, C. Cigolini et al. (2012). Radiative heat power at Stromboli volcano during 2000-2011: Twelve years of MODIS observations, J. Volcanol. Geoth. Res, 215-216, 48-60. doi:10.1016/j.jvolgeores.2011.12.001.

Coppola, D., D. Piscopo, T. Staudacher and C. Cigolini (2009). Lava discharge rate and effusive pattern at Piton de la Fournaise from MODIS data, J. Volcanol. Geoth. Res., 184, 1-2, 174-192, doi:10.1016/j.jvolgeores.2008.11.031.

Cordonnier, B., E. Lev and F. Garel (2016). Benchmarking lava-flow models, Geological Society, London, Special Publications, 426, 1, 425-445, doi:10.1144/SP426.7.

Corradini, S., S. Scollo, L. Guerrieri, L. Mereu et al. (2023). Volcanic plumes detection and retrievals from remote sensing systems: recent development and future improvements, 2023 International Conference on Electromagnetics in Advanced Applications (ICEAA), 488-488, doi:10.1109/ICEAA57318.2023.10297633.

Corradino, C., E. Amato, F. Torrisi and C. Del Negro (2022). Data-Driven Random Forest Models for Detecting Volcanic Hot Spots in Sentinel-2 MSI Images. Remote Sens-Basel, 14, 17, 4370, doi:10.3390/rs14174370.

Corradino, C., E. Amato, F. Torrisi, and C. Del Negro (2021). Towards an automatic generalized machine learning approach to map lava flows. 2021 17th International Workshop on Cellular Nanoscale Networks and their Applications (CNNA), 1-4, doi:10.1109/CNNA49188.2021.9610813.

Corradino, C., G. Ganci, A. Cappello, G. Bilotta et al. (2019). Mapping Recent Lava Flows at Mount Etna Using Multispectral Sentinel-2 Images and Machine Learning Techniques. Remote Sens-Basel, 11, 16, 1916, doi:10.3390/rs11161916.

Corradino, C., A. B. Malaguti, M. S. Ramsey and C. Del Negro (2024). Quantitative Assessment of Volcanic Thermal Activity from Space Using an Isolation Forest Machine Learning Algorithm. Remote Sens-Basel, 16(11), 2001. doi:10.3390/rs16112001.

Del Negro, C., E. Amato, F. Torrisi, C. Corradino et al. (2022). Support Vector Machine for volcano hazard monitoring from space at Mount Etna. 2022 IEEE 21st Mediterranean Electrotechnical Conference (MELECON), 627-631. doi:10.1109/MELECON53508.2022.9842942.

Del Negro, C., A. Cappello, G. Bilotta, G. Ganci et al. (2020). Living at the edge of an active volcano: Risk from lava flows on Mt. Etna, GSA Bulletin, 132, 7-8, 1615-1625, doi:10.1130/B35290.1.

Di Bella, G. S., C. Corradino, S. Cariello, F. Torrisi and C. Del Negro (2024). Advancing Volcanic Activity Monitoring: A Near-Real-Time Approach with Remote Sensing Data Fusion for Radiative Power Estimation, Remote Sens-Basel, 16, 16, 2879, doi:10.3390/rs16162879.

Harris, A. J. L. (2013). Thermal remote sensing of active volcanoes: a user's manual. Cambridge university press.

Harris, A. J. L., J. Dehn and S. Calvari (2007). Lava effusion rate definition and measurement: a review, Bull. Volcanol., 70, 1, 1-22. doi:10.1007/s00445-007-0120-y.

Harris, A. J. L., J. B. Murray, S. E. Aries, M. A. Davies et al. (2000). Effusion rate trends at Etna and Krafla and their implications for eruptive mechanisms, J. Volcanol. Geoth. Res, 102, 3-4, 237-269. doi:10.1016/S0377-0273(00)00190-6.

Harris, A. J. L., A. Steffke, S. Calvari and L. Spampinato (2011). Thirty years of satellite-derived lava discharge rates at Etna: Implications for steady volumetric output, J. Geophys. Res.: Solid Earth, 116, B8, B08204, doi:10.1029/2011JB008237.

Hérault, A., G. Bilotta, A. Vicari, E. Rustico and C. Del Negro (2011). Numerical simulation of lava flow using a GPU SPH model, Ann Geophys-Italy, 54, 5, doi:10.4401/ag-5343.

Jain, V., M. C. Biesinger, and M. R. Linford (2018). The Gaussian-Lorentzian Sum, Product, and Convolution (Voigt) functions in the context of peak fitting X-ray photoelectron spectroscopy (XPS) narrow scans, Appl. Surf. Sci., 447, 548-553, doi:10.1016/j.apsusc.2018.03.190.

James, G., D. Witten, T. Hastie and R. Tibshirani (2013). An introduction to statistical learning. Springer US.

Kapteyn, M. G. and K. E. Willcox (2020). From Physics-Based Models to Predictive Digital Twins via Interpretable Machine Learning (Versione 3). arXiv, doi:10.48550/ARXIV.2004.11356.

Malaguti, A. B., C. Corradino, A. La Spina, S. Branca and C. Del Negro (2024). Machine Learning Insights into the Last 400 Years of Etna Lateral Eruptions from Historical Volcanological Data, Geosciences, 14, 11, 295, doi:10.3390/geosciences14110295.

Monaghan, J. J. (1992). Smoothed particle hydrodynamics., Annu Rev Astron Astr, 30, 543-574, doi:10.1146/annurev.aa.30.090192.002551.

Monaghan, J. J. (2005). Smoothed particle hydrodynamics, Rep. Prog. Phys., 68, 8, 1703-1759, doi:10.1088/0034-4885/68/8/R01.

Monaghan, J. J. and A. Kos (1999). Solitary Waves on a Cretan Beach, J. Waterw. Port C, 125, 3, 145-155, doi:10.1061/(ASCE)0733-950X(1999)125:3(145).

Pioli, L., M. Palmas, B. Behncke, E. De Beni et al. (2022). Quantifying Strombolian Activity at Etna Volcano, Geosciences, 12, 4, 163, doi:10.3390/geosciences12040163.

Plank, S., F. Marchese, C. Filizzola, N. Pergola et al. (2019). The July/August 2019 Lava Flows at the Sciara del Fuoco, Stromboli-Analysis from Multi-Sensor Infrared Satellite Imagery. Remote Sens., 11, 23, 2879, doi:10.3390/rs11232879.

Plank, S., F. Massimetti, A. Soldati, K.-U. Hess et al. (2021). Estimates of lava discharge rate of 2018 Kīlauea Volcano, Hawai'i eruption using multi-sensor satellite and laboratory measurements, Int J. Remote Sens., 42, 4, 1492-1511, doi:10.1080/01431161.2020.1834165.

Saikali, E., G. Bilotta, A. Hérault and V. Zago (2020). Accuracy Improvements for Single Precision Implementations of the SPH Method, Int. J. Comput. Fluid D, 34, 10, 774-787, doi:10.1080/10618562.2020.1836357.

Scollo, S., L. Mereu, M. Prestifilippo and F. Romeo (2024). Characterization of Volcanic Plumes by Remote Sensing Sensors: An Example from Etna Volcano. IGARSS 2024 – 2024 IEEE International Geoscience and Remote Sensing Symposium, 3817-3820, doi:10.1109/IGARSS53475.2024.10642244.

Torrisi, F., E. Amato, C. Corradino and C. Del Negro (2023). The FastVRP automatic platform for the thermal monitoring of volcanic activity using VIIRS and SLSTR sensors: FastFRP to monitor volcanic radiative power, Ann Geophys-Italy, 65, 6, 1, doi:10.4401/ag-8823.

Torrisi, F., E. Amato, C. Corradino, S. Mangiagli and C. Del Negro (2022). Characterization of Volcanic Cloud Components Using Machine Learning Techniques and SEVIRI Infrared Images, Sensors, 22, 20, 7712, doi:10.3390/s22207712.

Torrisi, F., C. Corradino, S. Cariello and C. Del Negro (2024). Enhancing detection of volcanic ash clouds from space with convolutional neural networks, J. Volcanol. Geoth. Res., 448, 108046. doi:10.1016/j.jvolgeores.2024.108046.

Vicari, A., H. Alexis, C. Del Negro, M. Coltelli et al. (2007). Modeling of the 2001 lava flow at Etna volcano by a Cellular Automata approach, Environ. Modell. Softw., 22, 10, 1465-1471. doi:10.1016/j.envsoft.2006.10.005.

Vicari, A., G. Bilotta, S. Bonfiglio, A. Cappello et al. (2011). LAV@HAZARD: a web-GIS interface for volcanic hazard assessment, Ann Geophys-Italy, 54, 5, doi:10.4401/ag-5347.

Vugrin, K. W., L. P. Swiler, R. M. Roberts, N. J. Stucky-Mack and S. P. Sullivan (2007). Confidence region estimation techniques for nonlinear regression in groundwater flow: Three case studies, Water Resour. Res., 43, 3, 2005WR004804. doi:10.1029/2005WR004804.

Wadge, G. (1978). Effusion rate and the shape of aa lava flow-fields on Mount Etna, Geology, 6, 8, 503, doi:10.1130/0091-7613(1978)6<503:ERATSO>2.0.CO;2.

Wadge, G. (1981). The variation of magma discharge during basaltic eruptions, J. Volcanol. Geoth. Res., 11, 2-4, 139-168. doi:10.1016/0377-0273(81)90020-2.

Wendland, H. (1995). Piecewise polynomial, positive definite and compactly supported radial functions of minimal degree, Adv. Comput. Math., 4, 1, 389-396, doi:10.1007/BF02123482.

Wooster, M. J. (2003). Fire radiative energy for quantitative study of biomass burning: derivation from the BIRD experimental satellite and comparison to MODIS fire products, Remote Sens. Environ., 86, 1, 83-107. doi:10.1016/S0034-4257(03)00070-1.

Wooster, M. J., G. Roberts, G. L. W. Perry and Y. J. Kaufman (2005). Retrieval of biomass combustion rates and totals from fire radiative power observations: FRP derivation and calibration relationships between biomass consumption and fire radiative energy release, J. Geophys. Res-Atmos., 110, D24, 2005JD006318, doi:10.1029/2005JD006318.

Zago, V. (2018). Smoothed Particle Hydrodynamics method and flow dynamics: the case of lava numerical modeling and simulation (Ph.D. Thesis, Università degli studi di Catania). https://hdl.handle.net/20.500.14242/76328.

Zago, V., G. Bilotta, A. Cappello, R. A. Dalrymple et al. (2017). Simulating Complex Fluids with Smoothed Particle Hydrodynamics. Ann Geophys-Italy, 60(6 Sup), 1. doi:10.4401/ag-7362.

Zago, V., G. Bilotta, A. Cappello, R. A. Dalrymple et al. (2018). Preliminary validation of lava benchmark tests on the GPUSPH particle engine. Ann Geophys-Italy, 61, 2, doi:10.4401/ag-7870.

Zago, V., G. Bilotta, A. Hérault, R. A. Dalrymple et al. (2018). Semi-implicit 3D SPH on GPU for lava flows, J. Comp. Phys., 375, 854-870. doi:10.1016/j.jcp.2018.07.060.

Zago, V., L. J. Schulze, G. Bilotta, N. Almashan and R. A. Dalrymple (2021). Overcoming excessive numerical dissipation in SPH modeling of water waves, Coast. Eng., 170, 104018, doi:10.1016/j.coastaleng.2021.104018.

Zuccarello, F., G. Bilotta, A. Cappello and G. Ganci (2022). Effusion Rates on Mt. Etna and Their Influence on Lava Flow Hazard Assessment, Remote Sens., 14, 6, 1366, doi:10.3390/rs14061366.

Zuccarello, F., G. Bilotta, G. Ganci, C. Proietti and A. Cappello (2023). Assessing impending hazards from summit eruptions: the new probabilistic map for lava flow inundation at Mt. Etna. Sci Rep., 13, 1, 19543. doi:10.1038/s41598-023-46495-0.

***CORRESPONDING AUTHOR: Eleonora AMATO**,
Istituto Nazionale di Geofisica e Vulcanologia, Sezione di Catania, Osservatorio Etneo, Catania, Italy
e-mail: eleonora.amato@ingv.it